MMC Based Solid State Transformer for large-scale Distributed PV Integration and Medium Voltage AC/DC Interconnection

Saleh Farzamkia, Mafu Zhang, Huanghaohe Zou, Adithyan Vetrivelan, Alex Q. Huang, Fellow, IEEE.

Abstract—This paper proposes a novel multiport modular multilevel converter-based solid state transformer (MMC-SST) with a distributed control system architecture for large-scale PV integration and medium-voltage AC/DC interconnection. The distributed arrangement of PV arrays within the proposed topology enables the implementation of distributed maximum power point tracking (DMPPT), which mitigates the effects of partial shading and enhances energy harvesting from PV arrays. The symmetric design of the proposed MMC-SST eliminates the common power imbalance issue in MMC-based PV inverters. Additionally, the symmetric design of sub-MMC modules introduced in this paper makes it possible to suppress capacitor voltage ripples and differential currents effectively without the need for measuring arm currents. As a result, the proposed MMC-SST requires a smaller capacitor size, fewer current sensors, and lower isolated communications. Several case studies are conducted, and hardware-in-the-loop (HIL) simulation results are provided to validate the performance of the proposed MMC-SST and designed control system.

Index Terms--Distributed control system, MMC-SST, Modular Multilevel Converter (MMC), Power balance, PV inverter, Solid State Transformer (SST).

I. INTRODUCTION

Modular multilevel converter (MMC) is the most popular topology for interconnecting a medium voltage DC (MVDC) microgrid with the medium voltage AC (MVAC) grid [1], [2]. On the AC side, the MMC can be directly connected to the MVAC grid without needing a step-up transformer [3],[4]. Its common DC bus also enables the interconnection of the MVDC microgrid [5]. Additionally, the MMC contains several sub-modules (SMs) with floating capacitors that can be linked to PV arrays [6]. The distributed arrangement of PV arrays within the MMC and the implementation of distributed maximum power point tracking (DMPPT) can reduce the impacts of partial shading and enhance energy harvesting from the system [7]. However, this arrangement results in different power generation within SMs and leads to inter-module, inter-arm, and inter-phase power imbalances within the converter [6]-[8].

Several research are conducted in literature to mitigate the power imbalance issue in MMC-based PV systems that can be categorized into software-based and hardware-based methods [6]-[20]. In the software-based methods, the control systems are designed to transfer power from SMs with higher power generation to the other SMs with lower power generation [7]-[11]. For example, in reference [7], an energy-balancing strategy has been proposed to distribute total power among SMs, considering various power generation imbalances. Reference [8] has also proposed a control system to balance the internal energy of the MMC even during zero-power mode operation. However, transferring power from SMs with higher power generation to the other SMs with lower power generation increases the differential current within MMC. To mitigate inter-phase power imbalance, for example, a DC differential current is circulated among the phases, while the inter-arm power imbalance is mitigated by increasing the AC component of the differential currents [8], [10]. Increasing the differential current in MMC, however, results in a higher power loss and larger capacitor voltage ripple. Moreover, similar to the power imbalance issue in CHB-based PV systems with delta configuration [6], [12], the effectiveness of software-based methods is limited by the current rating of the devices.

In the hardware-based methods, modifications are made to the system configuration to prevent power imbalances within the converter [13]-[18]. For instance, reference [13] presents an interleaved MMC configuration with two DC links for SM-level PV integration. However, this configuration is not modular and does not fully match with the DMPPT concept. In [14], a hybrid MMC-based PV inverter is suggested with redundant SMs, where zero-sequence voltages are injected into phase voltages to address power imbalance issues. However, introducing zero-sequence voltages can lead to overvoltage problems in phases. Reference [15] employs a stabilizing module connected to batteries to manage partial shading conditions. This structure also does not utilize all modules for power generation, resulting in the under-utilization of SMs. Additionally, solving the inter-phase power imbalance issue still requires circulating a DC current within the converter that increases the power loss. Reference [16] has connected the primary side of all SMs to the same DC bus. However, this connection necessitates an additional DC-DC boost converter at the primary side of each SM. Reference [17] also proposed an MMC-based PV inverter including a DC bus for charging electric vehicles. This configuration effectively tackles inter-module and inter-phase power imbalances. However, for addressing inter-arm power imbalances, an AC circulating current flows in the arms, which results in higher power loss and larger capacitor voltage ripples. Furthermore, this configuration provides only one DC bus for PV integration.

In addition to the power imbalance issue, complexity of control system is another significant challenge for the implementation of MMC-based PV inverters. In large MMCs, numerous voltages and currents must be measured, multiple control algorithms need to be executed, and hundreds of control commands have to be generated. In the centralized control architecture, substantial computational power is required for

processing, and a wide communication bandwidth is essential for data exchange between the central controller and SMs. Wiring complexity and low reliability due to a single point of failure are other drawbacks of the centralized control system in large MMCs [19]. Distributed control architecture offers an alternative solution that can alleviate the processing load on the central controller and simplify the communication system's complexity [20]. The idea behind this architecture is to delegate some lower-level control tasks, such as MPPT, capacitor voltage balancing, and modulation, from the central controller to local controllers. For example, references [20]-[22] have proposed SM-based distributed control systems to shift the capacitor voltage balancing and differential current control to local controllers. However, utilization of these approaches necessitates advanced synchronization techniques to mitigate harmonics, voltage waveform distortions, and control conflicts [19]. References [23]-[25] have also categorized existing SMs in each arm into multiple clusters. Subsequently, a control module is designed to independently handle capacitor voltage balancing and modulation for each cluster. While these methods can effectively reduce the processing load of the central controller, they might not achieve the desired performance in smaller systems since reducing the number of SMs in the clusters affects both capacitor voltage balancing and voltage waveform quality.

This paper proposes a novel MMC-SST with a distributed control system architecture for large-scale PV integration and MVDC to MVAC interconnection. The distributed arrangement of PV arrays in the proposed MMC-SST enables the implementation of DMPPT and enhances the energy harvesting from PV arrays. The common power imbalance issue in MMC-based PV inverters is eliminated, and capacitor voltage ripples and differential currents are effectively suppressed due to a symmetrical design. To simplify the control system, the proposed MMC-SST is divided into sub-MMCs, and all lower-level control tasks are executed at the sub-MMC level through local controllers. Balanced power distribution, smaller capacitor size, fewer current sensors, and lower isolated communications are the main advantages of the proposed MMC-SST and distributed control system. Several case studies are considered, and Hardware-in-the-Loop (HIL) simulation results are provided to validate the performance of the proposed configuration and control system.

The remainder of this paper is structured as follows: Section II presents the basic operation principle and equivalent circuits of the MMC. Section III introduces and models the proposed MMC-SST. Section IV elaborates on the proposed distributed control system, encompassing the lower-level control system for the local controllers and the higher-level control tasks for the central controller. Section V considers several case studies, providing HIL simulation results for validation. Finally, Section VI presents the conclusions.

II. Basics of MMC and Equivalent Circuits

Fig. 1(a) shows the conventional structure of a three-phase MMC. As it can be seen, each phase of MMC contains two arms and each arm includes an inductor (L_{arm}) to regulate the arm current, a resistor (R_{arm}) to model the power loss, and N series connected SMs to generate N+1 voltage levels. Several

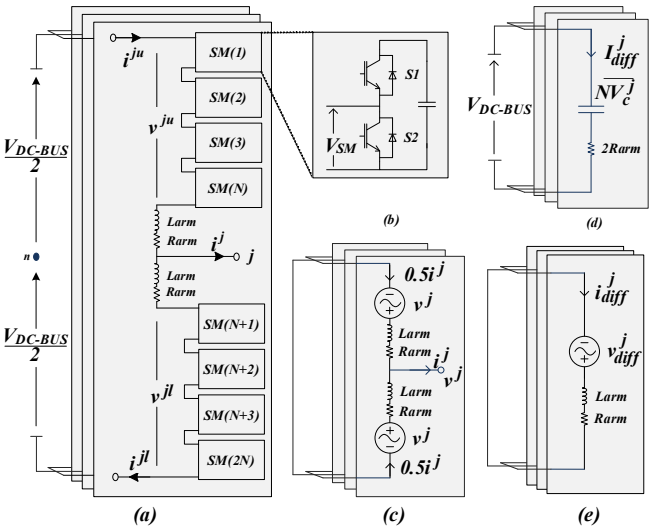

Fig. 1. (a) Typical configuration of three-phase MMC with N SMs per arm. (b) Structure of SMs. (c) Fundamental frequency equivalent circuit. (d) DC equivalent circuit. (e) Differential equivalent circuit.

structures are proposed for SMs, among which the half-bridge structure depicted in Fig. 1(b) is more common. During normal operation, each SM generates two voltage levels of 0 and $+V_c$. Hence, by N SMs per arm and disregarding higher order harmonics, the arm voltages can be written as:

$$v^{ju} = \frac{N\overline{V_c^{ju}}}{2} - V_{ref}\cos(\omega t + \varphi^j) \tag{1}$$

$$v^{j,l} = \frac{N\overline{V_c^{jl}}}{2} + V_{ref}\cos(\omega t + \varphi^j) \tag{2}$$

where v^{ju} and v^{jl} represents the upper and lower arm voltages of phase j respectively. The average capacitor voltages in the upper and lower arm of phase j are denoted by $\overline{V_c^{ju}}$ and $\overline{V_c^{jl}}$. The ω is the angular frequency, and φ^j is the initial angle in phase j. Indeed, V_{ref} is the reference voltage magnitude, which is defined as follows:

$$V_{ref} = m\frac{V_{DC-bus}}{2} \tag{3}$$

where m is the modulation index and V_{DC-bus} is the common DC bus voltage. The phase-to-neutral voltage of the converter is as follows:

$$v^j = V_{ref}\cos(\omega t + \varphi^j) \tag{4}$$

The KVL in upper and lower arms can be written as follows:

$$-\frac{V_{DC-Bus}}{2} + v^{ju} + L_{arm}\frac{di^{ju}}{dt} + R_{arm}i^{ju} + v^j = 0 \tag{5}$$

$$\frac{V_{DC-Bus}}{2} - v^{jl} - L_{arm}\frac{di^{jl}}{dt} - R_{arm}i^{jl} + v^j = 0 \tag{6}$$

where i^{ju} and i^{jl} are the upper and lower arm currents respectively. By subtracting equation (6) from equation (5) and substituting (1) and (2):

$$\frac{V_{DC-Bus}}{2} - \frac{N\overline{V_c^j}}{2} = L_{arm}\frac{d}{dt}\left(\frac{i^{ju}+i^{jl}}{2}\right) + R_{arm}\frac{i^{ju}+i^{jl}}{2} \tag{7}$$

where $\overline{V_c^j}$ represents the average capacitor voltage of phase j. The left-hand side of equation (7) is the differential voltage of phase j, which can be decomposed into DC and AC component:

$$\frac{V_{DC-Bus}}{2} - \frac{N\overline{V_c^j}}{2} = V_{diff}^j + v_{diff}^j \quad (8)$$

Similarly, the differential current of phase j can be defined as follows:

$$\frac{i^{j,u} + i^{j,l}}{2} = I_{diff}^j + i_{diff}^j \quad (9)$$

In this equation, I_{diff}^j and i_{diff}^j are the DC and AC components of the differential current in phase j. Based on these equations, the MMC can be modelled by a fundamental frequency equivalent circuit, a DC equivalent circuit, and a differential equivalent circuit, which are depicted in Fig. 1(c), Fig. 1(d), and Fig. 1(e), respectively.

III. Proposed MMC-SST Structure and Modelling

Fig. 2 demonstrates the overall configuration of the system under investigation, including an MVDC line for collecting offshore wind power and an MVAC line connecting the system to the main AC grid. The proposed MMC-SST primarily functions as an interconnecting converter between MVDC and MVAC lines. Additionally, it provides multiple isolated DC links for integrating distributed PV arrays. Unlike the conventional configuration where PV integration and AC/DC interconnection are handled by separate converters, the proposed MMC-SST combines both tasks. This integration reduces energy conversion stages and results in a more compact

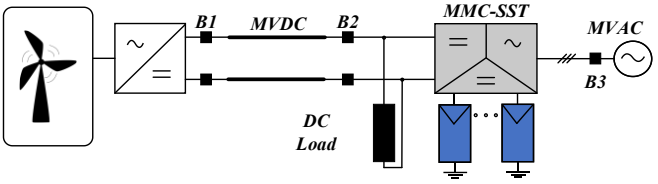

Fig. 2. Overall configuration of the system.

station footprint [2]. Moreover, the proposed configuration offers higher efficiency and a reduced number of devices compared to conventional systems [26]-[28].

Fig. 3 illustrates the detailed configuration of the proposed MMC-SST and its distributed control system. Each PV array is grounded to meet installation safety requirements. The left-hand side of the inverter is the upper arm, while the right-hand side forms the lower arm of the converter. As shown in Fig. 3, the proposed MMC-SST is comprised of sub-MMC modules, each consisting of six SMs located in six different arms of the converter. The primary side of all six SMs within a sub-MMC is connected to a PV array by isolated DC-DC converters. Each sub-MMC is also equipped with a local control system to handle lower-level control tasks. In addition to distributed DC terminals for PV integration at the sub-MMC level, the proposed configuration also includes medium voltage AC and DC terminals that are utilized for medium voltage AC/DC interconnections.

In order to model the proposed MMC-SST, similar to (1) and (2), the arm voltages of sub-MMC can be written as follows:

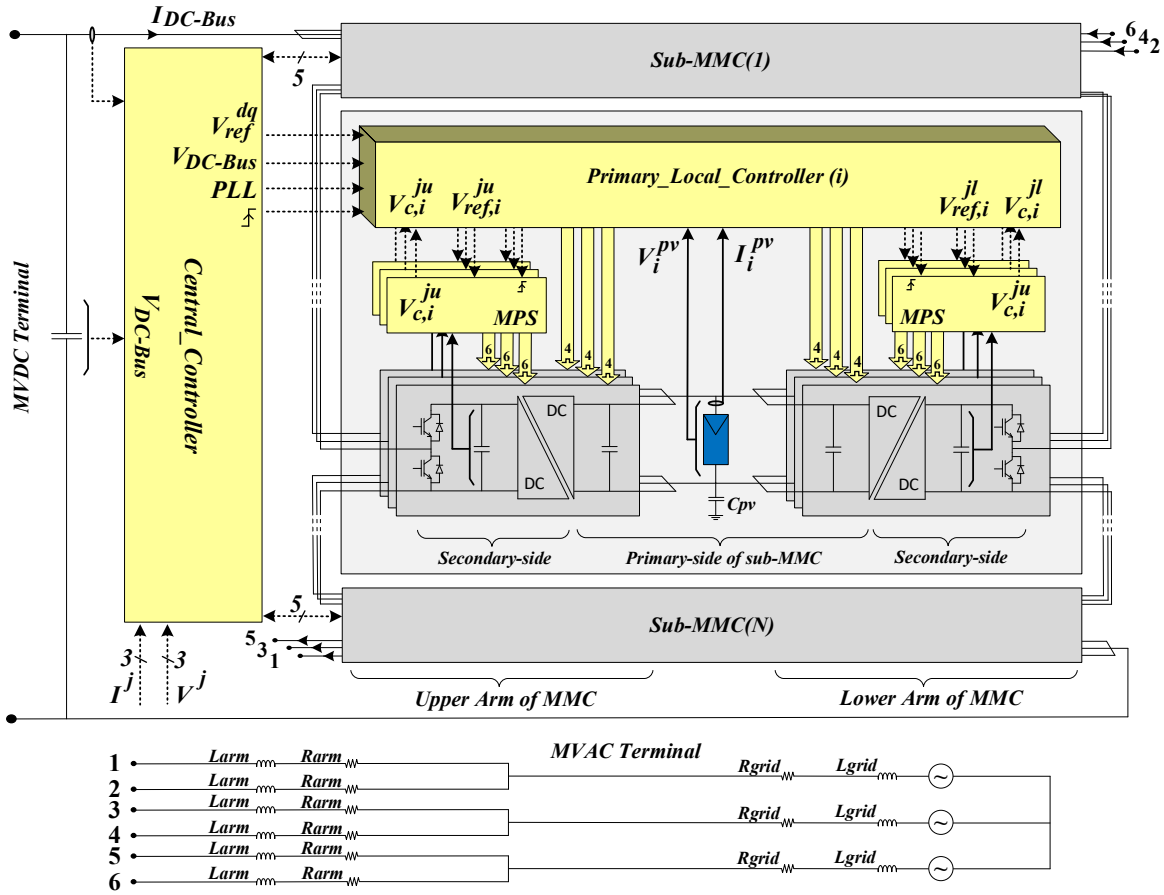

Fig. 3. The proposed configuration of MMC-SST PV inverter with distributed control system architecture.

$$v_i^{uj} = \frac{V_{c,i}^{ju}}{2} - V_{ref,i}cos(\omega t + \varphi^j) \quad (10)$$

$$v_i^{lj} = \frac{V_{c,i}^{jl}}{2} + V_{ref,i}cos(\omega t + \varphi^j) \quad (11)$$

where, $V_{c,i}^{ju}$ and $V_{c,i}^{jl}$ are the capacitor voltages in the upper and lower arm of phase j in the i^{th} sub-MMC, respectively. $V_{ref,i}$, also, is the reference voltage magnitude of the i^{th} sub-MMC that can be defined as follows:

$$V_{ref,i} = m_i \frac{V_{DC-bus}}{2N} \quad (12)$$

where, m_i is the modulation index of the i^{th} sub-MMC. Accordingly, the phase voltage of sub-MMC is:

$$v_i^j = V_{ref,i}cos(\omega t + \varphi^j) \quad (13)$$

The KVL in upper and lower arms can be written as follows:

$$\frac{V_{DC-Bus}}{2N} - \frac{\overline{V_{c,i}^J}}{2} = L_{arm}\frac{d}{dt}\left(\frac{i_i^{ju} + i_i^{jl}}{2}\right) + R_{arm}\left(\frac{i_i^{ju} + i_i^{jl}}{2}\right) \quad (14)$$

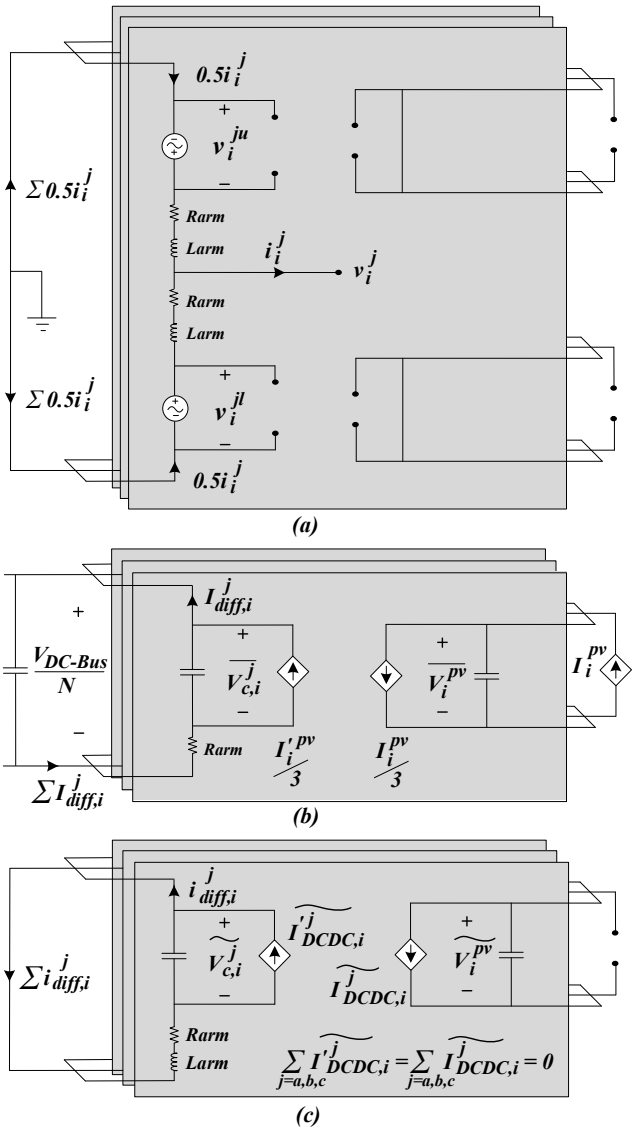

Fig. 4. Equivalent circuits of sub-MMC: (a) Fundamental frequency equivalent circuit. (b) DC equivalent circuit. (c) Differential equivalent circuit.

$$\frac{V_{DC-Bus}}{2N} - \frac{\overline{V_{c,i}^J}}{2} = V_{diff,i}^j + v_{diff,i}^j \quad (15)$$

where, i_i^{ju} and i_i^{jl} are the upper and lower arm currents, and $\overline{V_{c,i}^J}$ is the average capacitor voltage of phase j. The $V_{diff,i}^j$ and $v_{diff,i}^j$, also, are the DC and AC components of differential voltages of phase j. Similar to (9), the DC and AC components of differential currents of phase j are as follows:

$$I_{diff,i}^j + i_{diff,i}^j = \frac{i_i^{j,u} + i_i^{j,l}}{2} \quad (16)$$

Based on the derived formulations, the AC, DC, and differential equivalent circuits of the sub-MMC are depicted in

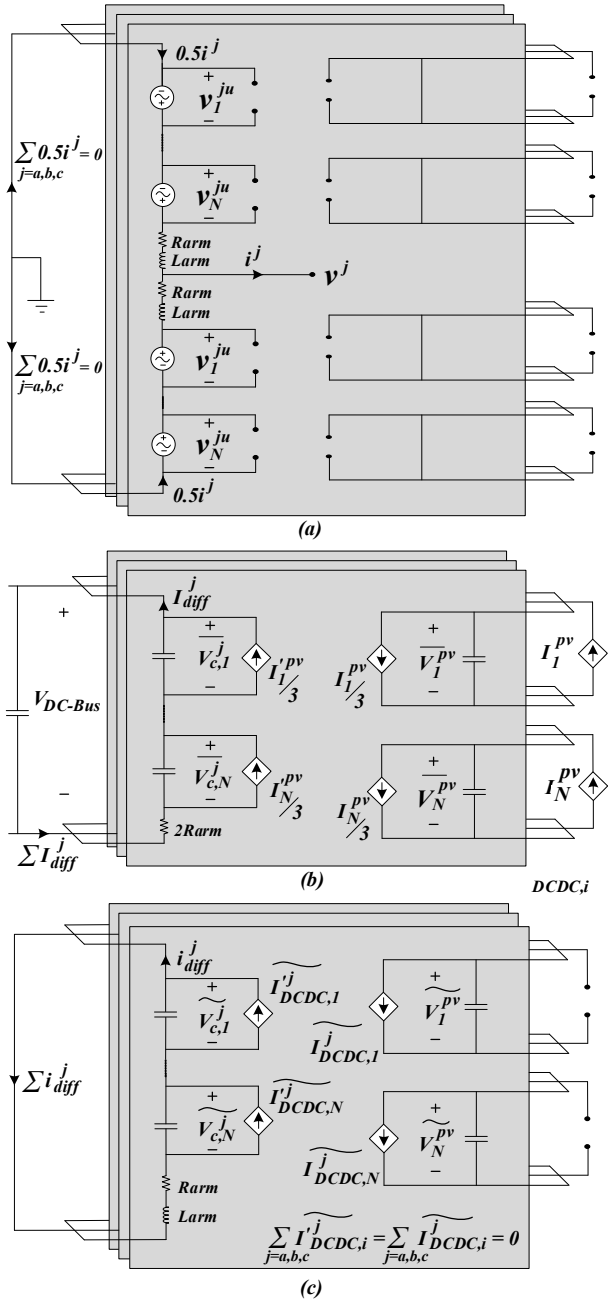

Fig. 5. Equivalent circuits of the proposed MMC-SST PV inverter: (a) Fundamental frequency equivalent circuit. (b) DC equivalent circuit. (c) Differential equivalent circuit.

Fig. 4(a), Fig. 4(b), and Fig. 4(c), respectively. The proposed configuration consists of N sub-MMCs that are connected in series to build-up the required voltage level. Based on the obtained models for sub-MMC, and using superposition theorem, the AC, DC, and the differential equivalent circuits of the inverter are demonstrated in Fig. 5(a), Fig. 5(b), and Fig. 5(c), respectively.

IV. Proposed Distributed Control System

As shown in Fig. 3, the proposed MMC-SST comprises a series connection of sub-MMCs, each equipped with local controllers. In the proposed distributed control system, lower-level control tasks are designed to be executed at the sub-MMC level, aiming to reduce the processing burden on the central controller and minimize the necessary communication. In this section, various components of the proposed control system are elaborated.

A. Distributed MPPT control in Sub-MMC

The centralized arrangement of PV arrays is highly susceptible to partial shading and module mismatches. In the proposed configuration, however, PV arrays have a distributed arrangement, allowing each sub-MMC to independently perform MPPT. The DMPPT control target is adjusting the PV voltages to their MPP voltages by controlling the phase-shifts in the isolated DC-DC converters. For this purpose, as shown in Fig. 6, the PV voltage and current are measured locally, and compared with the primary-side capacitor voltage reference that is generated by the MPPT algorithm. In this paper, the well-known perturb and observe (P&O) algorithm is utilized for MPPT. Subsequently, a PI controller generates the required phase-shift to convey the PV power from the primary-side to the secondary side of SMs. The phase-shift obtained in this step is identical for the six SMs of a sub-MMC. In Fig. 3, this part of the control system is implemented in the primary local controllers. Since the primary sides of SMs are connected to the same DC link, the primary local controllers indicated in Fig. 3 can measure PV voltage and current locally without isolation requirements.

B. Power Balancing within Sub-MMC

The DMPPT control generates identical phase shifts for the six SMs of a sub-MMC to transfer the PV power from the primary-side to the secondary-side. However, uniform phase shifts might result in different powers being transferred to SMs due to manufacturing tolerances. To ensure balanced power distribution among the SMs, secondary-side capacitor voltage controllers are required. The control target here is balancing the average voltage of the secondary-side capacitors, and this can be achieved by correcting the obtained phase-shift from the DMPPT control for each SM. For this purpose, according to Fig. 6, individual capacitor voltages are compared with the average secondary-side capacitor voltage of sub-MMC, and any disparity is corrected by a PI regulator. In this manner, the PV power is evenly distributed among SMs, and the inter-module, inter-arm, and inter-phase power imbalance problem disappears within the sub-MMCs. In Fig. 3, this part of the control system is implemented in the primary local controllers. The secondary-side capacitor voltages are measured locally by MPS microcontrollers and transmitted to the primary side controller using isolated communications.

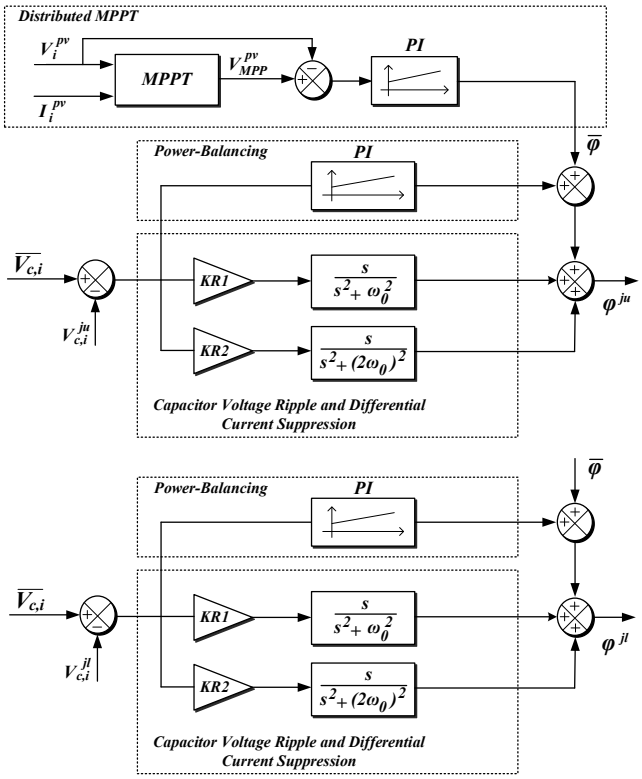

Fig. 6. DMPPT, power balancing, capacitor voltage ripple and differential current controllers in sub-MMC level.

C. Capacitor Voltage Ripple Cancellation in Sub-MMC

Applying power balancing control ensures that the secondary-side capacitors maintain the same average voltage. However, alongside this average voltage, a notable fundamental frequency ripple appears in the secondary-side capacitor voltages, significantly impacting the stability and performance of the converter. This voltage ripple results in waveform distortion, uneven voltage stress on components, and accelerated aging. In the proposed configuration, thanks to a symmetric design, this capacitor voltage ripple can be eliminated within sub-MMCs.

Disregarding higher-order harmonics, the upper and lower arm capacitor voltages of the MMC can be written as follows [29]:

$$V_{c,i}^{j,u} = \overline{V_{c,i}^{j}} - A\cos\left(\omega t + \alpha_1^{\,j}\right) - B\sin\left(2\omega t + \alpha_2^{\,j}\right) \tag{17}$$

$$V_{c,i}^{j,l} = \overline{V_{c,i}^{j}} + A\cos\left(\omega t + \alpha_1^{\,j}\right) - B\sin\left(2\omega t + \alpha_2^{\,j}\right) \tag{18}$$

where, A and B are the first and second harmonic coefficients, and $\alpha_1^{\,j}$ and $\alpha_2^{\,j}$ are their initial angles. In order to eliminate the fundamental frequency ripple of the capacitor voltage, aside from the DC current, the DC-DC converter introduces a fundamental frequency current into the secondary-side capacitor. This AC current lags 90 degrees behind the fundamental frequency of the capacitor voltage ripple. Consequently, according to the superposition theorem, it generates an additional fundamental frequency voltage, which lags 180 degrees behind the fundamental frequency ripple of the capacitor voltage. Hence, it counteracts the existing

capacitor voltage ripple and neutralizes it. The required AC current is generated by a proportional-resonant (PR) controller with a fundamental frequency, as depicted in Fig. 6. This controller introduces an AC component to the previously obtained DC phase-shift to eliminate the fundamental frequency ripple of capacitor voltage.

The most important point here is that according to (17) and (18), the fundamental frequency component of capacitor voltages in the upper and lower arms are complementary. Therefore, the compensating AC currents for the upper and lower arm SMs are also complementary. Since the primary side of SMs are connected to the same DC link, the compensating AC currents of the upper and lower arm SMs cancel each other automatically at the primary side. Therefore, the secondary side ripple cancellation is achieved without affecting the primary-side capacitor voltage since the total primary-side current remains constant. It is important to note that the fundamental frequency ripple is the main factor for sizing capacitors in MMC, and elimination of this ripple significantly reduces the required capacitor size in this converter. In Fig. 3, this part of the control system is implemented in the primary local controller without needing additional communications.

D. Differential Current Control in Sub-MMC

In addition to the fundamental frequency ripple, the capacitor voltage of MMC contains a double-frequency component according to (17) and (18). Although the double-frequency component is significantly smaller, its elimination is still crucial because it is the primary source of the double-frequency component of the differential currents [20]. In the MMC applications, this component circulates within the converter and increases the power loss. In order to suppress the double-frequency component of the differential current, similar to the fundamental frequency ripple cancellation, a double-frequency PR controller is added to the controller in Fig. 6. This PR controller introduces a double frequency current into the secondary-side capacitor voltage to neutralize its double-frequency voltage ripple.

The key point here is that the double-frequency ripple of capacitors in different phases exhibits a 120-degree phase-shift. Consequently, the compensating currents in these phases also possess a 120-degree phase shift. As the primary sides of SMs within each sub-MMC are connected to the same DC link, these compensating currents effectively cancel each other on the primary side as a balanced three-phase system. Therefore, the second-harmonic component of the differential current can be eliminated at the sub-MMC level without requiring any current sensors. In Fig. 3, this part of the control system is implemented in the primary local controller without needing additional communications.

E. Higher-Level Control System

In the proposed MMC-SST, the higher-level control system is designed to manage power flow between terminals and coordinate sub-MMCs. In the system depicted in Fig. 2, the MMC-SST collects the generated PV powers from sub-MMCs and maintains power balance between the MVDC and MVAC grids. Regulating the common DC bus voltage is the primary function of the higher-level control system. By controlling this voltage, the MVDC link current can be adjusted, and remaining

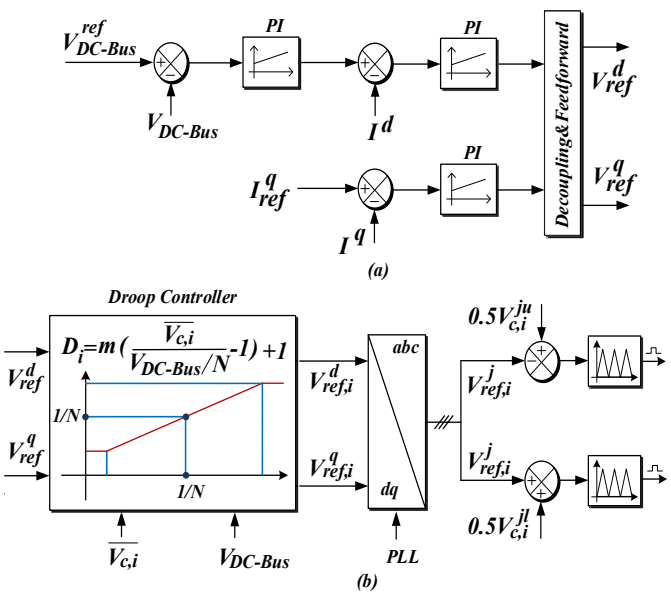

Fig. 7. (a) The higher-level control system of the proposed configuration. (b) Sharing reference voltage among sub-MMCs.

power automatically flows into the MVAC grid. Fig. 7(a) illustrates the higher-level control system for MMC-SST, employing conventional voltage-oriented control (VOC) to regulate the common DC bus voltage and generate the reference voltage for MMC-SST. This part of the control system as well as system-level protections are implemented in the central controller, and resulting reference voltages are transmitted to the local controllers as shown in Fig. 3.

F. Sharing Reference Voltage among Sub-MMCs

In the previous section, the higher-level control system generates overall reference voltages for the entire converter. These reference voltages need to be distributed among the series-connected sub-MMCs. Due to their series connection, the currents in the sub-MMCs are identical. When the overall reference voltage is divided among these sub-MMCs, their voltages also become uniform. Consequently, different sub-MMCs process the same power, despite differences in their PV powers. In such a condition, the average capacitor voltage of sub-MMCs with higher power generation increases, and potentially leads to converter instability. Therefore, it is essential to allocate the overall reference voltage among sub-MMCs in proportion to their PV power. To achieve this, referring to Fig. 4(a) and using equation (13), the sub-MMC's power at the AC side can be calculated as follows:

$$P_i^{ac} = \sum_{j=a,b,c} v_i^j \times i^j = \frac{3}{2} V_{ref,i} . I_m \cos(\varphi_0) \tag{19}$$

where $\cos(\varphi_0)$ represents the power factor. Using Fig. 4(b), the DC-side power of sub-MMC, also can be calculated as follows:

$$P_i^{DC} = \frac{1}{T} \int_{t_0}^{T+t_0} \overline{V_{c,i}} \times \sum_{j=a,b,c} \left(I_{diff,i}^j - \frac{I_i'^{pv}}{3} \right) dt = \Psi\left(I_{diff,i}^j, V_{PV,i}, \varphi_i, \dots \right) \times \overline{V_{c,i}} \tag{20}$$

where $\overline{V_{c,i}}$ represents the average capacitor voltage of i[th] sub-MMC. By neglecting the power loss, the average power on both

the DC and AC sides of each sub-MMC should be equal in steady-state conditions. Therefore, from (19) and (20):

$$\overline{V_{c,i}} = \frac{\frac{3}{2} I_m \cos(\varphi_0)}{\Psi\left(I^{j,diff}, V_{PV,i}, \dots\right)} V_{ref,i} \tag{21}$$

This equation reveals a linear correlation between the average capacitor voltage and the reference voltage amplitude of the sub-MMC. As a PV array generates more power, the average capacitor voltage of that sub-MMC increases. To maintain power balance between the DC and AC sides, according to (21), the reference voltage magnitude of that sub-MMC should be proportionally increased. Based on this linear correlation, a droop controller is designed to distribute the overall reference voltage among sub-MMCs in proportion to their average capacitor voltages in Fig. 7(b). The designed droop controller automatically allocates a larger portion of the reference voltage to the sub-MMC with higher PV power generation. In Fig. 3, this segment of the control system is also implemented in the primary local controller. The overall reference voltages, along with the common DC bus voltage, are transmitted from the central control to the primary side controller using isolated communications.

G. *Merits of Proposed Distributed Control system*

As discussed in the introduction section, implementing DMPPT in MMC-based PV inverters can lead to inter-module, inter-arm, and inter-phase power imbalances. The proposed MMC-SST addresses this issue through the symmetric design of sub-MMCs. In this configuration, each PV array is linked to a sub-MMC comprising six SMs positioned in six different arms. Through the proposed distributed control system, the PV power is evenly shared among the SMs which results in a homogeneous power distribution within the entire converter.

The capacitor voltage ripple cancellation is another advantage of the proposed configuration, which can significantly reduce the required capacitor size. This cancellation occurs because the capacitor voltage ripples within the sub-MMC are complementary, and their compensating currents cancel each other at the primary side.

Moreover, the proposed differential current control is implemented locally without the need for measuring the arm currents. In existing distributed control systems [20]-[25], the arm currents are measured by central controllers. In [23]-[25], the differential current controllers are executed in the central controllers, whereas in [20]-[22], both the measured differential current and its DC reference are transmitted from the central controller to the local controllers. In the proposed distributed control system, the need for arm current sensors is eliminated. Instead, as depicted in Fig. 6, the proposed differential current control relies on the secondary-side capacitor voltages, which are already measured. Consequently, the proposed differential current controller reduces the requirement for current sensors and communication within the system.

The local controller within the sub-MMC can be implemented by a single processor. However, it should be noted that the secondary side of the SMs is isolated from the primary side. Therefore, all communication signals between the primary and secondary side must be isolated. In the distributed control systems, there is a desire to minimize isolated communication signals due to their higher cost and vulnerability to noise. For this purpose, a DSP processor can be utilized for the primary side of the sub-MMC and a cost-effective single-dollar MPS microcontroller for the secondary side of each SM. The primary-side controller receives communication signals from the central controller and executes the lower-level control tasks. The MPS controllers also receive the arm voltage reference and perform modulation. By doing so, the gate signals shown in Fig. 3 can be generated locally without isolated communication.

TABLE I
HIL SIMULATION SYSTEM PARAMETERS

Parameter	Value
Rated power of MMC-SST	2 MW
Rated line-to-line voltage of AC microgrid (rms)	4.2 kV
Rated voltage of MVDC microgrid	10 kV
Sensitive DC load power	300 kW
Number of sub-MMCs	3
Number of MPPTs	3
AC microgrid filter	1 mH
MVDC line impedance	5 Ω, 100 mH
Nominal voltage of SMs	3.3 kV
Capacitance of SMs	500 uF
Arm inductance	2 mH
Arm resistance	0.2 Ω
DC fault resistance	0.5 Ω

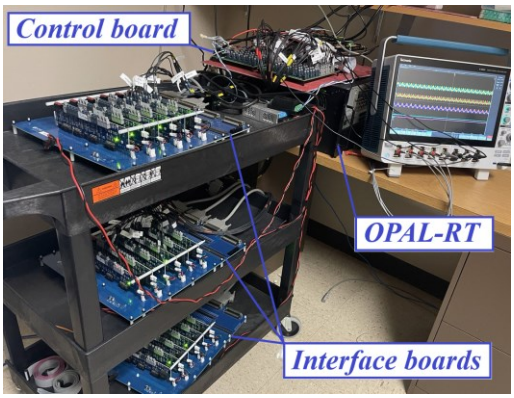

Fig. 8. HIL simulation setup.

V. HARDWARE-IN-THE LOOP SIMULATION RESULTS

To validate the performance of the proposed configuration and distributed control system, multiple case studies were examined, and HIL simulation results are presented. In Fig. 8, the experimental setup is depicted, including OPAL-RT, control board, and interface boards. The implemented system comprises three sub-MMCs connected to three PV arrays. Detailed parameters of the implemented system are provided in Table I. The MMC-SST is implemented in the OPAL-RT using a switching model. For the offshore wind farm, also, an average model is utilized. Due to the limitations of our setup, various parts of the proposed control system are implemented as separate blocks within the central controller. To emulate a distributed control system, communications among these blocks are restricted to the signals depicted in Fig. 3.

The first case study is designed to investigate the performance of the lower-level control system. In this experiment, each PV array generates 330 kW, and the power of the offshore wind farm is 1 MW. Figs. 8 and 9 illustrate the internal voltages and currents within a sub-MMC before and after enabling the proposed lower-level control system. Before activating the controller, as evident in Fig. 9, there are significant ripples in the secondary-side capacitor voltages.

Upon enabling the controller, as shown in Fig. 10, fundamental and double-frequency currents are introduced to the secondary-side capacitors, leading to the elimination of capacitor voltage ripples. Fig. 11 also displays the upper and lower arm currents, along with the differential current within the converter. It is noticeable that, with the controller enabled, the double-frequency component of the differential current disappears.

Furthermore, Fig. 9 illustrates that the fundamental frequency ripples at the upper and lower arms are complementary before activating the controllers. As shown in Fig. 10, the compensating currents become complementary for the upper and lower arm SMs after the controllers are enabled. Consequently, the compensating currents automatically nullify each other, leading to a consistent total current on the primary side and a constant capacitor voltage. Fig. 13 also presents the droop coefficients for sub-MMCs. Given that PV powers are identical in this experiment, the droop coefficients are also equal, as expected.

In the second case study, we explore the performance of the designed droop controller under unequal power generation from PV arrays. As indicated in Fig. 14, the power generation of the first PV array is increased from 330 kW to 430 kW, while the second PV array's power generation is reduced from 330 kW to 200 kW. Fig. 15 presents the step power response at the primary side of the first sub-MMC. It is evident that with the increase in PV power, both the PV current and the DC component of the primary side currents also rise. By injecting more power into the SMs, as depicted in Fig. 16, the average capacitor voltage of the first sub-MMC increases. Consequently, the droop controller allocates a larger portion of the reference voltage to the first sub-MMC. Conversely, the lower power generation in the second sub-MMC results in a lower average capacitor voltage and a smaller droop coefficient. Fig. 17 also shows the DC bus voltage, DC bus current, differential current, AC grid currents, and arm currents during this test.

To investigate the effects of droop adjustment on the system's performance, the same test is conducted with a smaller "m." As demonstrated in Fig. 18, reducing "m" has decreased the sensitivity of the controller to variations in average capacitor voltages. Indeed, decreasing "m" resulted in a slower dynamic response of the average capacitor voltage controller.

In the third case study, the system's performance is tested under a DC fault scenario. Prior to the fault occurrence, the MVDC line in Fig. 2 transfers 1 MW of wind power at a voltage of 10 kV. The DC fault is introduced to the middle of the MVDC line with a 0.5-ohm fault resistance. After 15 ms, the fault is cleared by opening DC circuit breakers B1 and B2. Following this event, the MMC-SST functions as an uninterruptible power supply (UPS) for the DC load that is connected to its common DC bus. Fig. 19 illustrates the obtained results during the DC fault. Before the fault condition, the common DC bus current is approximately 70A. During post-fault operation, the common DC bus voltage is restored after a short transient period. The common DC bus current also reaches -30A. The negative current here indicates that power is flowing from the common DC bus to the DC load. Additionally, the remaining PV power is delivered to the MVAC grid, as shown in Fig. 19.

The final case study investigates the system's performance during islanding mode operation. In this test, the proposed

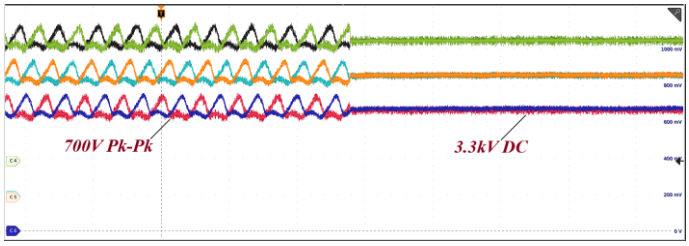

Fig. 9. Secondary side capacitor voltages before and after enabling the proposed lower-level control system.

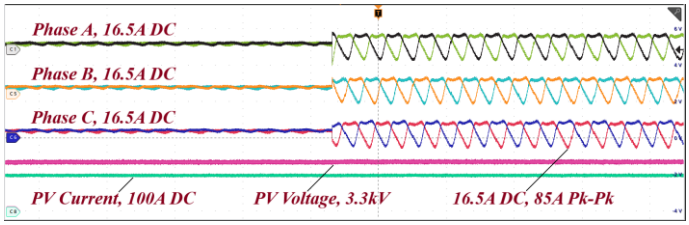

Fig. 10. PV voltage, PV current, and primary side currents of SMs before and after enabling the proposed lower-level control system.

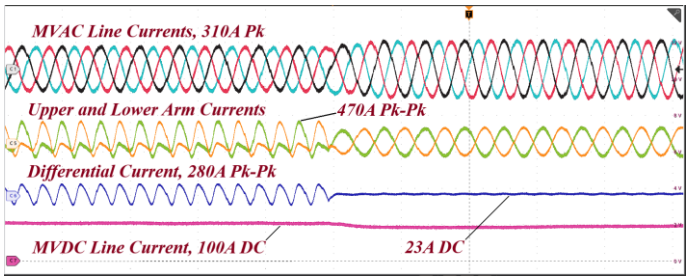

Fig. 11. AC side currents, arm currents, differential current, and DC side current before and after enabling the lower-level control system.

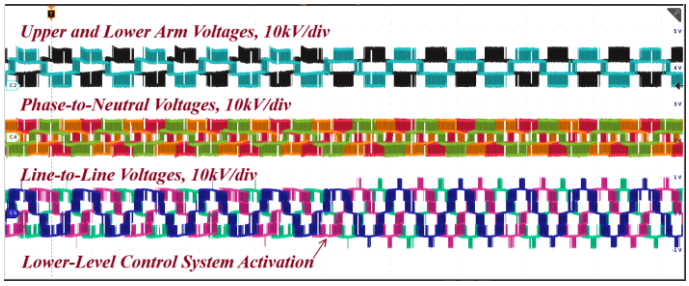

Fig. 12. Arm voltages, phase-to-neutral voltages, and line-to-line voltages before and after enabling the lower-level control system.

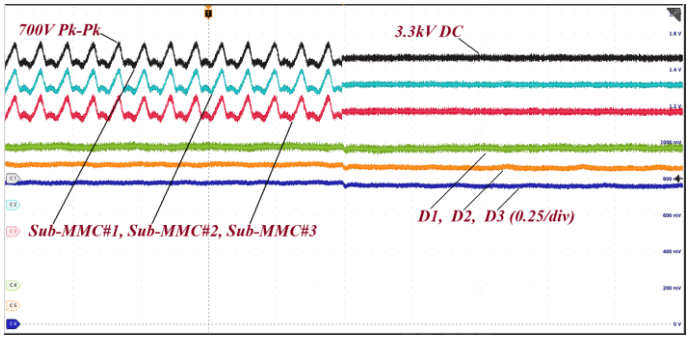

Fig. 13. SM capacitor voltages and droop coefficients before and after enabling the lower-level control system ($m = 5$).

MMC-SST is disconnected from the main AC grid by opening AC circuit breaker B3. However, the common DC bus remains connected to the DC load and the MVDC line. In this situation,

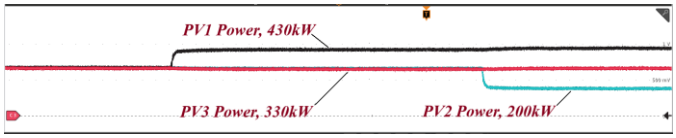

Fig. 14. Step changes at the first and second PV power generation.

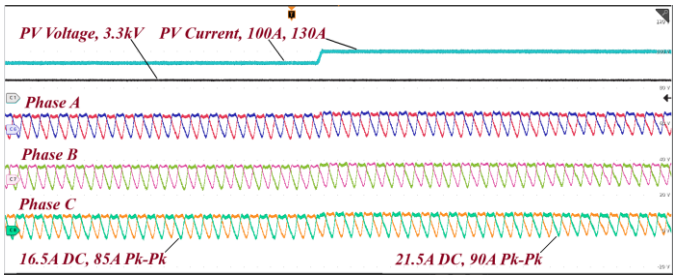

Fig. 15. PV voltage, PV current, and primary side SM currents during step change in PV power generation.

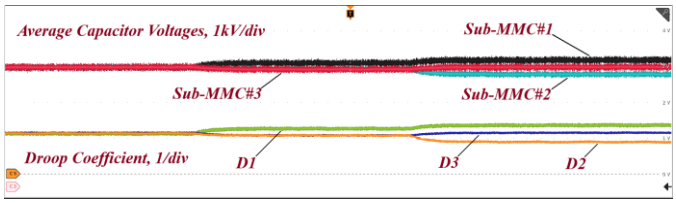

Fig. 16. Average capacitor voltages and droop coefficients ($m = 5$).

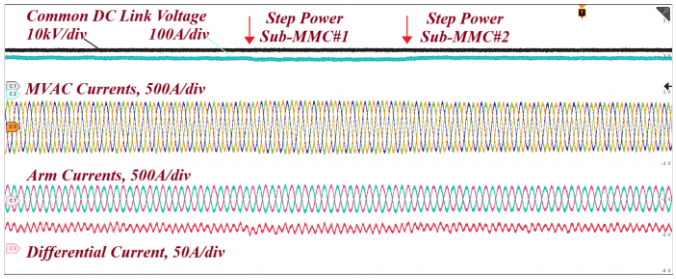

Fig. 17. DC side voltage and current, differential current, AC side currents, and arm currents during second case study.

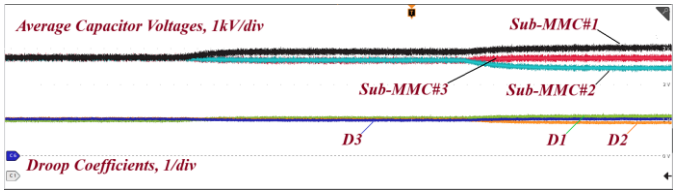

Fig. 18. Average capacitor voltages and droop coefficients ($m = 1$).

the generation capacity of the islanded section is much higher than the DC load. Consequently, the system cannot continue to operate with MPPT, and it needs to switch to constant power mode. Fig. 20 and 21 demonstrate the obtained results for islanding mode operation. At the beginning of the islanding mode, the generated power exceeds the load consumption, leading to an increase in the common DC bus voltage. However, after bypassing the MPPTs, power generation and consumption are balanced, and the common DC bus voltage returns to 10 kV. The common DC bus current has also reached -30A, indicating that the load is fully supplied by the MMC-SST, and the MVDC line current is nearly zero. The droop coefficients of the sub-MMCs are also depicted in Fig. 21. As

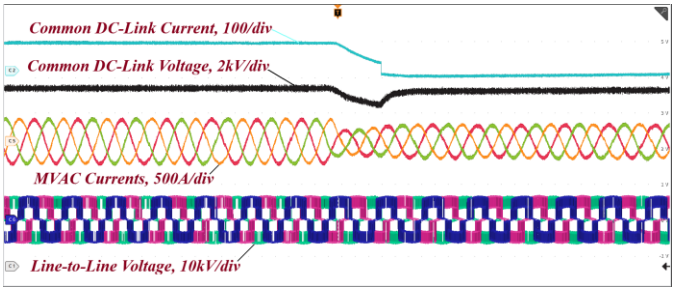

Fig. 19: Results obtained before and after applying a DC fault.

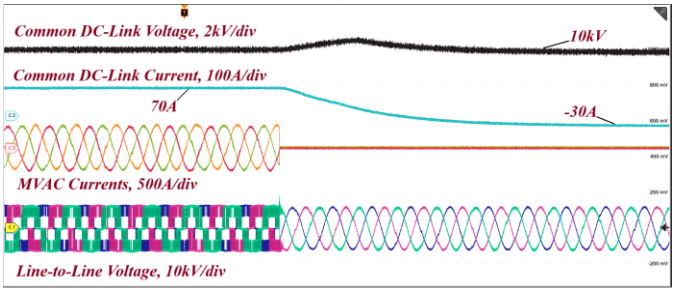

Fig. 20: Results obtained from islanding mode operation.

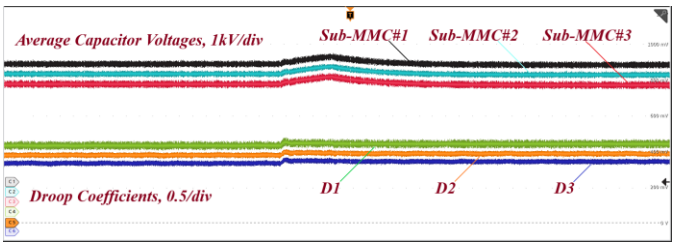

Fig. 21. Average capacitor voltages and droop coefficients during islanding mode operation.

the PV arrays generate equal power, the droop coefficients and their variations are the same, as anticipated.

The results obtained from several case studies validate the performance of the proposed MMC-SST and distributed control system. Across various scenarios, such as lower-level control system performance, unequal power generation from PV arrays, DC fault conditions, and islanding mode operation, the system consistently demonstrated efficient and reliable operation.

VI. CONCLUSIONS

In conclusion, the proposed MMC-SST with distributed control architecture represents a significant advancement in integrating large-scale PV systems and medium-voltage AC/DC interconnection. By distributing PV arrays among sub-MMCs and implementing DMPPT, our method mitigates the negative effects of partial shading and enhances energy harvesting from PV arrays. The symmetric design of sub-MMCs effectively eliminates the common inter-module, inter-arm, and inter-phase power imbalances in MMC-based PV inverters. This configuration enables effective suppression of capacitor voltage ripples, leading to a reduction in required capacitor size. Additionally, implementing local differential current control without the need for arm current sensors streamlines system design and reduces the complexity of communication within the distributed control system. Through comprehensive case studies and HIL simulations, we have

demonstrated the effectiveness of the proposed MMC-SST and distributed control system architecture. Overall, the proposed MMC-SST with distributed control system offers a promising solution for enhancing the reliability, cost-effectiveness, and performance of large-scale PV integration and medium-voltage AC/DC interconnection systems.

REFERENCES

[1] L. Zhang, Y. Tang, S. Yang and F. Gao, "Decoupled Power Control for a Modular-Multilevel-Converter-Based Hybrid AC–DC Grid Integrated With Hybrid Energy Storage," in IEEE Transactions on Industrial Electronics, vol. 66, no. 4, pp. 2926-2934, April 2019, doi: 10.1109/TIE.2018.2842795.

[2] M. Rouhani and G. J. Kish, "Multiport DC–DC–AC Modular Multilevel Converters For Hybrid AC/DC Power Systems," in IEEE Transactions on Power Delivery, vol. 35, no. 1, pp. 408-419, Feb. 2020, doi: 10.1109/TPWRD.2019.2927324.

[3] S. Farzamkia, M. Noushak, H. Iman-Eini, A. Khoshkbar-Sadigh and S. Farhangi, "Fault-Tolerant Method to Reduce Voltage Stress of Submodules in Postfault Condition for Regenerative MMC-Based Drive," in *IEEE Transactions on Industrial Electronics*, vol. 68, no. 6, pp. 4718-4726, June 2021, doi: 10.1109/TIE.2020.2991998.

[4] S. Farzamkia, H. Iman-Eini, M. Noushak and A. Hadizadeh, "Improved Fault-Tolerant Method for Modular Multilevel Converters by Combined DC and Neutral-Shift Strategy," in IEEE Transactions on Industrial Electronics, vol. 66, no. 3, pp. 2454-2462, March 2019, doi: 10.1109/TIE.2018.2823659.

[5] Xiao Q, Mu Y, Jia H, Jin Yu, Hou K, Yu X, et al. Modular multilevel converter based multi-terminal hybrid AC-DC microgrid with improved energy control method. Appl Energy 2021;282:116154.

[6] A. B. Acharya, M. Ricco, D. Sera, R. Teoderscu and L. E. Norum, "Performance Analysis of Medium-Voltage Grid Integration of PV Plant Using Modular Multilevel Converter," in IEEE Transactions on Energy Conversion, vol. 34, no. 4, pp. 1731-1740, Dec. 2019, doi: 10.1109/TEC.2019.2930819.

[7] Elsanabary, A., Mekhilef, S., Seyedmahmoudian, M., Stojcevski, A.: An energy balancing strategy for modular multilevel converter based grid-connected photovoltaic systems. IET Power Electron. 14, 2115–2126 (2021). https://doi.org/10.1049/pel2.12113

[8] B. E. d. O. B. Luna, C. B. Jacobina and A. C. Oliveira, "Internal Energy Balance of a Modular Multilevel Cascade Converter Based on Chopper-Cells With Distributed Energy Resources for Grid-Connected Photovoltaic Systems," in IEEE Transactions on Industry Applications, vol. 59, no. 2, pp. 1935-1943, March-April 2023, doi: 10.1109/TIA.2022.3225122.

[9] S. Barcellona, M. Barresi and L. Piegari, "MMC-Based PV Three-Phase System With Distributed MPPT," in IEEE Transactions on Energy Conversion, vol. 37, no. 3, pp. 1567-1578, Sept. 2022, doi: 10.1109/TEC.2022.3167786.

[10] Liu, P., Zhan, X., Wang, F., Jiang, T., Yu, C.: Unbalanced power control of a modular multilevel converter with photovoltaic resources and the capacitor voltage ripple analysis. IET Power Electron. 15, 701–716 (2022). https://doi.org/10.1049/pel2.12260

[11] H. Bayat and A. Yazdani, "A Power Mismatch Elimination Strategy for an MMC-Based Photovoltaic System," in IEEE Transactions on Energy Conversion, vol. 33, no. 3, pp. 1519-1528, Sept. 2018, doi: 10.1109/TEC.2018.2819982.

[12] A. I. Elsanabary, G. Konstantinou, S. Mekhilef, C. D. Townsend, M. Seyedmahmoudian and A. Stojcevski, "Medium Voltage Large-Scale Grid-Connected Photovoltaic Systems Using Cascaded H-Bridge and Modular Multilevel Converters: A Review," in IEEE Access, vol. 8, pp. 223686-223699, 2020, doi: 10.1109/ACCESS.2020.3044882.

[13] F. M. Alhuwaishel, A. K. Allehyani, S. A. S. Al-Obaidi and P. N. Enjeti, "A Medium-Voltage DC-Collection Grid for Large-Scale PV Power Plants With Interleaved Modular Multilevel Converter," in IEEE Journal of Emerging and Selected Topics in Power Electronics, vol. 8, no. 4, pp. 3434-3443, Dec. 2020, doi: 10.1109/JESTPE.2019.2934736.

[14] F. Rong, X. Gong and S. Huang, "A Novel Grid-Connected PV System Based on MMC to Get the Maximum Power Under Partial Shading Conditions," in IEEE Transactions on Power Electronics, vol. 32, no. 6, pp. 4320-4333, June 2017, doi: 10.1109/TPEL.2016.2594078.

[15] Malekjamshidi, Z. and Jafari, M. (2021), Design and development of a cascaded modular multi-level converter based on current-fed quadruple-active bridge converters for grid integration of photovoltaic systems. IET Energy Syst. Integr, 3: 26-38. https://doi.org/10.1049/esi2.12002

[16] K. Wang, R. Zhu, C. Wei, F. Liu, X. Wu and M. Liserre, "Cascaded Multilevel Converter Topology for Large-Scale Photovoltaic System With Balanced Operation," in IEEE Transactions on Industrial Electronics, vol. 66, no. 10, pp. 7694-7705, Oct. 2019, doi: 10.1109/TIE.2018.2885739.

[17] Y. -C. Su, H. -M. Li, P. -L. Chen and P. -T. Cheng, "Integration of PV Panels and EV Chargers on the Modular Multilevel Converter Based SST," in IEEE Transactions on Industry Applications, vol. 58, no. 5, pp. 6428-6437, Sept.-Oct. 2022, doi: 10.1109/TIA.2022.3189969.

[18] C. Liu, L. Wen, D. Yang, H. Ying, C. Liu and H. Zhang, "Two-type single-stage isolated modular multilevel cascaded converter (I-M2C2) topologies," in CPSS Transactions on Power Electronics and Applications, vol. 4, no. 1, pp. 10-18, March 2019, doi: 10.24295/CPSSTPEA.2019.00002.

[19] J. Na, H. Kim, S. Kim, C. -K. Kim, H. A. Mantooth and K. Hur, "Interleaving Clusters of Submodules to Enhance Scalability of Modular Multilevel Converters for High-Voltage Applications," in IEEE Transactions on Power Delivery, doi: 10.1109/TPWRD.2023.3291403.

[20] S. Yang, Y. Tang and P. Wang, "Distributed Control for a Modular Multilevel Converter," in IEEE Transactions on Power Electronics, vol. 33, no. 7, pp. 5578-5591, July 2018, doi: 10.1109/TPEL.2017.2751254.

[21] H. Wang, S. Yang, H. Chen, X. Feng and F. Blaabjerg, "Synchronization for an MMC Distributed Control System Considering Disturbances Introduced by Submodule Asynchrony," in IEEE Transactions on Power Electronics, vol. 35, no. 12, pp. 12834-12845, Dec. 2020, doi: 10.1109/TPEL.2020.2993284.

[22] B. Çiftçi, L. Harnefors, X. Wang, J. Gross, S. Norrga and H. -P. Nee, "Wireless Control of Modular Multilevel Converter Submodules With Communication Errors," in IEEE Transactions on Industrial Electronics, vol. 69, no. 11, pp. 11644-11653, Nov. 2022, doi: 10.1109/TIE.2021.3125664.

[23] M. Alharbi, S. Isik and S. Bhattacharya, "A Novel Submodule Level Fault-Tolerant Approach for MMC With Integrated Scale-Up Architecture," in IEEE Journal of Emerging and Selected Topics in Industrial Electronics, vol. 2, no. 3, pp. 343-352, July 2021, doi: 10.1109/JESTIE.2021.3061954.

[24] M. Alharbi and S. Bhattacharya, "Scale-Up Methodology of a Modular Multilevel Converter for HVdc Applications," in IEEE Transactions on Industry Applications, vol. 55, no. 5, pp. 4974-4983, Sept.-Oct. 2019, doi: 10.1109/TIA.2019.2925055.

[25] B. Xia et al., "Decentralized Control Method for Modular Multilevel Converters," in IEEE Transactions on Power Electronics, vol. 34, no. 6, pp. 5117-5130, June 2019, doi: 10.1109/TPEL.2018.2866258.

[26] S. Ansari, A. Chandel and M. Tariq, "A Comprehensive Review on Power Converters Control and Control Strategies of AC/DC Microgrid," in IEEE Access, vol. 9, pp. 17998-18015, 2021, doi: 10.1109/ACCESS.2020.3020035.

[27] S. Farzamkia, H. S. Rizi, A. Q. Huang and H. Iman-Eini, "Shared Redundancy Strategy to Improve the Reliability and Fault-Tolerant Capability of Modular Multilevel Converter," in IEEE Transactions on Industrial Electronics, vol. 70, no. 4, pp. 3326-3336, April 2023, doi: 10.1109/TIE.2022.3181416.

[28] Y. Li and G. J. Kish, "Comparative Assessment of Multi-Port MMCs for High-Power Applications," in IEEE Access, vol. 10, pp. 22049-22060, 2022, doi: 10.1109/ACCESS.2022.3152536.

[29] B. Li, Y. Zhang, G. Wang, W. Sun, D. Xu and W. Wang, "A Modified Modular Multilevel Converter With Reduced Capacitor Voltage Fluctuation," in IEEE Transactions on Industrial Electronics, vol. 62, no. 10, pp. 6108-6119, Oct. 2015, doi: 10.1109/TIE.2015.2423665.

Saleh Farzamkia (Graduate Student Member, IEEE) received the B.S. degree from Bu-Ali Sina University, Hamedan, Iran, in 2013, and the M.Sc. degree from the University of Tehran, Tehran, Iran, in 2015, both in electrical engineering with honors. He is currently pursuing a PhD with the Semiconductor Power Electronics Center (SPEC) at The University of Texas at Austin. His research interests include design, control, and applications of multilevel converters, reliability engineering, and fault-tolerance.

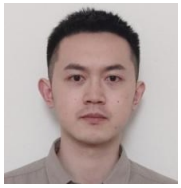

Mafu Zhang (Graduate Student Member, IEEE) received the B.S. degree from Xi'an Jiaotong University in 2017, and the M.Sc. degree from ETH Zürich in 2021, both in electrical engineering. He is currently pursuing a Ph.D. degree with the Semiconductor Power Electronics Center (SPEC) at The University of Texas at Austin, Austin, TX, USA. His research interests include AC-DC isolated converters and their modeling and control.

Huanghaohe Zou (Graduate Student Member, IEEE) received the B.S. degree in electrical engineering from Xi'an Jiaotong University, Xi'an, China in 2019. He is currently working towards the Ph.D. degree in electrical & computer engineering with Semiconductor Power Electronics Center (SPEC), the University of Texas at Austin, Austin, TX, USA. His research interests include single stage ac-dc converter, resonant converter and wide-band-gap power electronics. He is the recipient of two Best Presentation Awards at IEEE Applied Power Electronics Conference and Exposition (APEC) in 2023 and 2024, respectively.

Adithyan Vetrivelan (Graduate Student Member, IEEE) was born in Chennai, India. He received his bachelor's degree in electrical engineering from the College of Engineering Guindy (CEG), Anna University, Chennai, in 2017. He is currently pursuing a Ph.D. degree with the Semiconductor Power Electronics Center (SPEC) at The University of Texas at Austin, Austin, TX, USA. His research interests include the application of wide bandgap semiconductors in power electronics and the control of power electronics circuits.

Alex Q. Huang (Fellow, IEEE) was born in Zunyi, Guizhou, China. He received the B.Sc. degree in electrical engineering from Zhejiang University, Hangzhou, China, in 1983, the M.Sc. degree in electrical engineering from the Chengdu Institute of Radio Engineering, Chengdu, China in 1986, and the Ph.D. degree from Cambridge University, Cambridge, U.K., in 1992.

From 1992 to 1994, he was a Research Fellow at the Magdalene College, Cambridge University. From 1994 to 2004, he was a Professor with the Bradley Department of Electrical and Computer Engineering, Virginia Polytechnic Institute and State University, Blacksburg, VA, USA. From 2004 to 2017, he was the Progress Energy Distinguished Professor of electrical and computer engineering at NC State University, Raleigh, NC, USA, where he established and led the NSF FREEDM Systems Center. Since 2017, he has been the Dula D. Cockrell Centennial Chair in Engineering at The University of Texas at Austin, Austin, TX, USA. Since 1983, he has been involved in the development of modern power semiconductor devices and power integrated circuits. He fabricated the first IGBT power device in China, in 1985. He is the inventor and key developer of the emitter turn-off (ETO) thyristor. He developed the concept of energy Internet and the smart transformer-based energy router technology. He has mentored and graduated more than 80 Ph.D. and master students, and has published more than 500 articles in international conferences and journals. He has also been granted more than 20 U.S. patents. His current research interests are power electronics, power management microsystems, and power semiconductor devices.

Dr. Huang is a fellow of the National Academy of Inventors. He was a recipient of the NSF CAREER Award, the prestigious R&D 100 Award, the MIT Technology Review's 2011 Technology of the Year Award, and the 2019 IEEE Industry Applications Society (IAS) Gerald Kliman Innovator Award.